IOP Conf. Series: Materials Science and Engineering **418** (2018) 012002 doi:10.1088/1757-899X/418/1/012002

Crystal Plasticity Based Transformation Induced Plasticity Formulation for Predictions of Forming Limit Diagrams

P Zhang[1], CP Kohar[1], A Brahme[1], S-H Choi[2], RK Mishra[3], K Inal[1]

[1] Department of Mechanical and Mechatronics Engineering, University of Waterloo, Waterloo, Ontario, Canada, N2L 3G1
[2] Department of Printed Electronics Engineering, Sunchon National University, Sunchon, Jeonnam, Republic of Korea, 540-950
[3] General Motors Research and Development Center, 20500 Mound Road, Warren, MI, USA, 48090-9055

Email: kinal@uwaterloo.ca

Abstract. Significant effort has been invested into the development and research of Advanced High Strength Steel. In particular, transformation induced plasticity (TRIP) steel has shown promise as a candidate for lightweighting of vehicles because of their enhanced formability. However, predictive modeling of TRIP steel in formability is difficult due the combination of dislocation and transformation mechanisms occurring during deformation for various strain paths. This work presents a crystal plasticity constitutive model to simulate the behaviour of deformation induced $\gamma \rightarrow \alpha$' transformation. A physics based transformation model is implemented into the crystal plasticity framework to fully capture the behavior of TRIP assisted steels. Simulations are calibrated and compared to experimental measurements of Duplex Stainless Steel. The calibrated model is then used to predict the forming limit diagram using the Marciniak-Kuczynski approach. The results highlight the importance of a physics based used in simulation to fully utilize TRIP assisted steels.

1. Introduction

Transformation induced plasticity (TRIP) steel is a unique classification of advanced high strength steel (AHSS) where retained metastable austenite, γ, transforms into martensite, α', upon mechanical deformation [1]. Taking advantage of the TRIP mechanism, TRIP steels often offer substantially higher work hardening rates, tensile strength and strain elongation when compared to conventional high strength steel and other AHSS. As such, TRIP steel is an excellent candidate to reduce the weight of formability limited components on a vehicle [2]. To utilize these materials, the development of accurate simulation tools is critical to its successful deployment in the automotive industry.

The micro-scale polycrystalline plasticity model, also known as crystal plasticity, is a physics-based model [3] [4], which computes the crystallographic slip resulting from dislocation glide on individual crystal lattices [5]. The cumulative sum of all the different crystal orientations comprises the texture of the overall material. Initial texture bias naturally gives rise to anisotropy due to the readily available slip systems in specific directions. Upon initiation of dislocation glide, the crystal lattice will shear and accumulate dislocations through plastic strain. During the deformation process, the orientation of the crystals will change due to lattice rotation, leading to an evolution of the microstructure and anisotropy. In a material like steel, the main deformation mechanism is dislocation glide at room temperature, which is a fairly well understood mechanism. However, the TRIP mechanism observed in AHSS is complex;

Content from this work may be used under the terms of the Creative Commons Attribution 3.0 licence. Any further distribution of this work must maintain attribution to the author(s) and the title of the work, journal citation and DOI.
Published under licence by IOP Publishing Ltd

the underlying driving force of martensite transformation is a thermodynamic process. Bain and Dunkirk [6] proposed that this transformation at the lattice level distorts and rotates the FCC structure of austenite into a BCC structure of martensite through a shear mechanism. Scheil [7] proposed that shear stress on the habit planes is the mechanism that activated martensite transformation in austenite. A shear dislocation on the habit plane in the [111] direction is called fault bands. The FCC crystal has a total of 12 fault band systems. The intersection of fault bands from different habit planes creates a highly favorable site for the formation of martensite.

As such, constitutive modeling of TRIP assisted steel still requires substantial attention to capture the macro and micro-mechanical behavior in simulations of large deformation, let alone predict the formability of these materials. The Marciniak and Kuczynski (MK) [8] method offers an efficient framework for the calculation of forming limit diagrams (FLDs) for predicting formability. As of late, many formability analyses using the MK approach do not account for the physics of martensite transformation or martensite transformation in general [9], let alone the differences due to the microstructural phenomenon. Even with all the advancements in computational performance and experimentation, there still exists a need for a framework to quickly and efficiently simulate forming limits diagrams that accounts for the micromechanics of TRIP-assisted steels.

This work presents a micro-scale predictive simulation tool to capture the TRIP mechanism from austenite to martensite in multiphase AHSS for predicting formability. The proposed transformation framework will take advantage of the micro-scale physics and trigger transformation based on an evolving transformation criteria that can be related to several physical phenomena observed in experiments. The successful implementation of the proposed model will then be used to simulate the mechanical response of a duplex stainless steel (70% ferrite, 30% austenite). Once calibrated, the Marciniak and Kuczynski (MK) [8] framework will be used to calculate forming limit diagrams (FLDs) to evaluate formability of this TRIP-assisted steel.

2. Constitutive Model

This work assumes that ferrite and martensite have a body center cubic (BCC) structure [10], while austenite is assumed to be a face center cubic (FCC) structure. The BCC crystalline is assumed to have 24 slip systems active and that slip system activity is independent of temperature. The orientation relationship between parent phase and transformed martensite is assumed to follow a single variant of the Bain relationship. The transformation criterion is inspired by that of Kim et al. [11], however it has been modified as a stress based transformation criterion to suit the nature of a Taylor-type model. The framework uses a Taylor-type averaging scheme with rate-tangent modulus for time integration [12] to simulate the bulk deformation behavior of a polycrystal representative volume element (RVE).

2.1 Single Crystal Hardening Model

Deformation of a crystal is caused by crystallographic slip, through dislocation motion on active slip systems, and elastic lattice distortion and rigid body rotations of the lattice [3]. As such these deformations can be obtained through polar decomposition of the deformation gradient

$$\boldsymbol{F} = \boldsymbol{F}^{*}\boldsymbol{F}^{P} \tag{1}$$

where $\boldsymbol{F}$ is the deformation gradient, $\boldsymbol{F}^{P}$, accounts for crystallographic slip and $\boldsymbol{F}^{*}$, accounts for rigid body rotations and elastic deformation. The vectors $\boldsymbol{s}^{(\alpha)}$ and $\boldsymbol{m}^{(\alpha)}$ are regarded as lattice vectors such that they stretch and rotate by

$$\boldsymbol{s}^{*\,(\alpha)} = \boldsymbol{F}^{*}\boldsymbol{s}^{(\alpha)}, \qquad \boldsymbol{m}^{*\,(\alpha)} = \boldsymbol{m}^{(\alpha)}\boldsymbol{F}^{*-1} \tag{2}$$

The spatial gradient of velocity $\boldsymbol{L}$ is written as

$$\boldsymbol{L} = \dot{\boldsymbol{F}}\boldsymbol{F}^{-1} = \boldsymbol{L}^{*} + \boldsymbol{L}^{P} \tag{3}$$

where $\boldsymbol{L}^{P}$, accounts for crystallographic slip and component $\boldsymbol{L}^{*}$, accounts for rigid body rotations and elastic deformation. The symmetric strain rate tensor, $\boldsymbol{D}$, and skew symmetric spin tensor, $\boldsymbol{W}$, can be obtained from the velocity gradient

$$\boldsymbol{D} = \boldsymbol{D}^{*} + \boldsymbol{D}^{P} = \frac{1}{2}(\boldsymbol{L} + \boldsymbol{L}^{T}), \qquad \boldsymbol{W} = \boldsymbol{W}^{*} + \boldsymbol{W}^{\boldsymbol{P}} = \frac{1}{2}(\boldsymbol{L} - \boldsymbol{L}^{T}) \tag{4}$$

where $()^*$ and $()^P$ correspond to the isolation of the elastic and plastic components. The plastic component of the strain-rate and spin for the crystal can be respectively written as

$$\boldsymbol{D}^P = \sum_{\alpha} \boldsymbol{P}^{(\alpha)} \dot{\gamma}^{(\alpha)}, \quad \boldsymbol{W}^P = \sum_{\alpha} \boldsymbol{W}^{(\alpha)} \dot{\gamma}^{(\alpha)} \tag{5}$$

where $\dot{\gamma}^{(\alpha)}$ is the shear rate on each slip system α. The expansion of the symmetric and skew-symmetric tensors for each slip system α are written as

$$\boldsymbol{P}^{(\alpha)} = \frac{1}{2}\left[\boldsymbol{s}^{*(\alpha)} \otimes \boldsymbol{m}^{*(\alpha)} + \boldsymbol{m}^{*(\alpha)} \otimes \boldsymbol{s}^{*(\alpha)}\right] \tag{6}$$

$$\boldsymbol{W}^{(\alpha)} = \frac{1}{2}\left[\boldsymbol{s}^{*(\alpha)} \otimes \boldsymbol{m}^{*(\alpha)} - \boldsymbol{m}^{*(\alpha)} \otimes \boldsymbol{s}^{*(\alpha)}\right] \tag{7}$$

The constitutive model can be written in terms of the Jaumann rate of Cauchy stress through

$$\overset{\nabla}{\boldsymbol{\sigma}} = \mathbb{L}^{\boldsymbol{el}}\boldsymbol{D} - \dot{\boldsymbol{\sigma}}^0 - \boldsymbol{\sigma} \boldsymbol{tr} \boldsymbol{D} \tag{8}$$

where $\mathbb{L}^{\boldsymbol{el}}$ is the rotated 4th order elastic moduli tensor and $\dot{\boldsymbol{\sigma}}^0$ is the visco-plastic stress rate which is defined as

$$\dot{\boldsymbol{\sigma}}^0 = \sum_{\boldsymbol{\alpha}} \left(\mathbb{L}^{\boldsymbol{el}}\boldsymbol{P}^{(\alpha)} + \boldsymbol{W}^{(\alpha)}\boldsymbol{\sigma} - \boldsymbol{\sigma}\boldsymbol{W}^{(\alpha)}\right)\dot{\gamma}^{(\alpha)} \tag{9}$$

The slip rates formulated in the framework is the power-law relation

$$\dot{\gamma}^{(\alpha)} = \dot{\gamma}_{\boldsymbol{0}} sgn\left(\boldsymbol{\tau}^{(\alpha)}\right)\left|\frac{\boldsymbol{\tau}^{(\alpha)}}{\boldsymbol{g}^{(\alpha)}}\right|^{\frac{1}{m}} \tag{10}$$

$\dot{\gamma}_0 = 1.0 \times 10^{-3} s^{-1}$ is a reference shear rate (taken to be the same for all the slip systems), m is the strain-rate sensitivity exponent, $\boldsymbol{\tau}^{(\alpha)}$ is the resolved shear stresses and $\boldsymbol{g}^{(\alpha)}$ is the hardness of each slip system. The resolved shear stresses on each slip system $\boldsymbol{\tau}^{(\alpha)}$, is calculated using Schmid's Law

$$\boldsymbol{\tau}^{(\alpha)} = \boldsymbol{P}^{(\alpha)} : \boldsymbol{\sigma} \tag{11}$$

The rate of hardness increase of a crystal evolves based on $\dot{\boldsymbol{g}}^{(\alpha)}$ which is defined by the hardening law

$$\dot{\boldsymbol{g}}^{(\alpha)} = \sum_{\boldsymbol{\beta}} h_{(\alpha\beta)}\left|\dot{\gamma}^{(\boldsymbol{\beta})}\right| \tag{12}$$

where $h_{(\alpha\beta)}$ are the hardening moduli. Asaro and Needleman [3] proposed that the hardening moduli be defined as

$$h_{(\alpha\beta)} = q_{(\alpha\beta)} h_{(\beta)} \quad \text{(no sum on } \beta\text{)} \tag{13}$$

where $h_{(\beta)}$ is the hardening rate on a single slip system, and $q_{(\alpha\beta)}$ is a matrix that relates the latent hardening matrix of a slip system to the self-hardening rate. For a FCC crystal, the latent hardening matrix, $q^{FCC}_{(\alpha\beta)}$, is defined as

$$q^{FCC}_{(\alpha\beta)} = \begin{bmatrix} A & qA & qA & qA \\ qA & A & qA & qA \\ qA & qA & A & qA \\ qA & qA & qA & A \end{bmatrix} \tag{14}$$

A is a 3 x 3 unity matrix, and q is the latent hardening coefficient. In the above, slip systems {1,2,3} are coplanar, as are systems {4,5,6}, {7,8,9}, and {10,11,12}. Thus, the ratio of the latent-hardening rate to the self-hardening rate for coplanar systems are taken as unity. For a BCC crystal, the slip systems {1,2}, {3,4}, {5,6}, {7,8}, {9,10}, and {11,12} are coplanar while, slip systems 13-24 are of independent slip planes. Thus, the latent hardening matrix for a BCC crystal, $q^{BCC}_{(\alpha\beta)}$, is defined as

$$q_{(\alpha\beta)}^{BCC} = \begin{bmatrix} B & qB & qB & qB & qB & qB & \dots & \\ qB & B & qB & qB & qB & qB & & \\ qB & qB & B & qB & qB & qB & & \\ qB & qB & qB & B & qB & qB & & qC \\ qB & qB & qB & qB & B & qB & & \\ qB & qB & qB & qB & qB & B & & \\ \dots & & & & & & \dots & \\ & & & qC & & & & C \end{bmatrix} \quad (15)$$

where B is a 2 x 2 unity matrix and C is a 12 x 12 unity matrix. The power law hardening model is used to describe the hardening behaviour

$$h_{(\beta)} = h_0 \left(\frac{h_0 \gamma_a}{\tau_0 n} + 1 \right)^{n-1} \quad (16)$$

where h_0 is the initial hardening rate of the system, τ_0 is the initial critically resolved shear stress, n is the crystal hardening exponent and γ_a is the total accumulated slip defined by

$$\gamma_a = \int_0^t \sum_{\alpha} \left| \dot{\gamma}^{(\alpha)} \right| dt \quad (17)$$

2.2 Transformation Criteria

Martensite transformation is assumed to occur at the intersection of shear fault bands. Inspired by Kim et al. [11], the fault band shear stress triggers the proposed transformation criterion. An instance of transformation occurs when the resolved shear stress on two or more of the twelve habit plane systems exceeds the transformation threshold, Γ^{th}, defined as

$$\Gamma^{th} = C_{t1} + C_{t2} \cdot \Gamma^{acc} \quad (18)$$

where C_{t1}, C_{t2} are material parameters, and Γ^{acc} is the accumulated shear of the crystal. The accumulated slip Γ^{acc}, is the integration of the summation of the shear rates over time

$$\Gamma^{acc} = \int_0^t \left(\sum_{\alpha}^{N} \dot{\gamma}^{(\boldsymbol{\alpha})} \right) dt \quad (19)$$

Similarly, the resolved shear stress is calculated on each of the fault band systems, α, using Schmid's Law (equation) for every austenite crystal

$$\boldsymbol{\tau}^{\boldsymbol{HP}\,(\alpha)} = \boldsymbol{P}^{\boldsymbol{HP}\,(\alpha)} : \boldsymbol{\sigma} \quad (20)$$

where $\boldsymbol{P}^{\boldsymbol{HP}\,(\alpha)}$ is calculated on the habit plane indices. When two or more components of $\boldsymbol{\tau}^{\boldsymbol{HP}\,(\alpha)}$ exceeds that of Γ^{th} transformation is modelled to take place. Table 1 summarizes the 12 fault band systems in FCC (austenite) crystals.

Table 1. FCC fault band systems

α	Fault band systems	α	Fault band systems	α	Fault band systems
1	$[112] \otimes (11\bar{1})$	**5**	$[121] \otimes (1\bar{1}1)$	**9**	$[211] \otimes (\bar{1}11)$
2	$[1\bar{1}2] \otimes (1\bar{1}\bar{1})$	**6**	$[1\bar{2}1] \otimes (111)$	**10**	$[2\bar{1}1] \otimes (11\bar{1})$
3	$[11\bar{2}] \otimes (111)$	**7**	$[12\bar{1}] \otimes (1\bar{1}\bar{1})$	**11**	$[21\bar{1}] \otimes (1\bar{1}1)$
4	$[1\bar{1}\bar{2}] \otimes (1\bar{1}1)$	**8**	$[1\bar{2}\bar{1}] \otimes (11\bar{1})$	**12**	$[2\bar{1}\bar{1}] \otimes (111)$

Following the Bain orientation relationship, the newly formed BCC crystal lattice is rotated about the $< 001 >$ crystal axis by 45° that follows the single variant Bain relationship, such that

$$\boldsymbol{Q}^{\boldsymbol{trans}} = \boldsymbol{Q}_{t+1}(\phi_1 + 45°, \Phi, \phi_2) \quad (21)$$

and the orientation of the BCC slip systems $\boldsymbol{s}_{\boldsymbol{0}}^{\boldsymbol{BCC}}$ replace the FCC slip systems, $\boldsymbol{s}_{\boldsymbol{t+1}}^{*\,\boldsymbol{FCC}}$ such that

$$\boldsymbol{s}_{t+1}^{*} = \boldsymbol{Q}^{\boldsymbol{trans}} \boldsymbol{s}_{\boldsymbol{0}}^{\boldsymbol{BCC}} \quad (22)$$

Finally, the power-law hardening parameters of martensite are mapped over to replace the austenite parameters $\left(h_0^{\gamma}, \tau_0^{\gamma}, n^{\gamma} \rightarrow h_0^{\alpha'}, \tau_0^{\alpha'}, n^{\alpha'}\right)$ and the accumulated shear on each slip is reinitialized

$$\gamma_{t+1}^{(\alpha)} = 0 \quad (23)$$

3. Forming Limit Calculations

The framework for crystal plasticity MK analysis is developed by Wu et al. [13], and used by Inal et al. [14] is employed in this work. Figure 1 presents a schematic of the theoretical model used in the MK framework. The theoretical model assumes a smooth continuous variation in the thickness region of sheet material called a band, "b". This band is oriented at an angle, Ψ_0, concerning the principal axis with an initial thickness, t_0^b. The region outside of the band, known hereon as region, "a", is assumed to have initial uniform thickness, t_0^a.

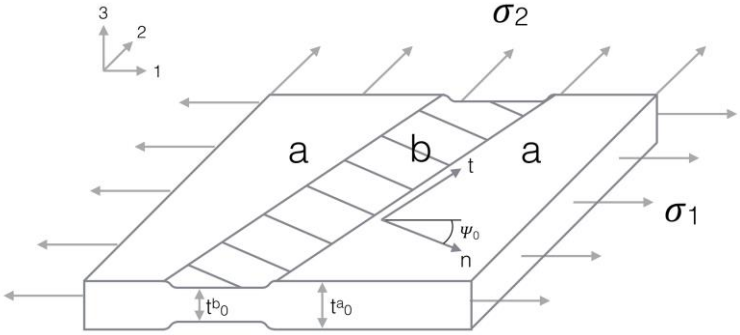


Figure 1. Geometrical model of the Marciniak-Kuczynski theory [8]

The initial imperfection parameter, f, which is known as the coefficient of geometrical non-homogeneity, is the ratio of band thickness $(\,)^b$ and the bulk material $(\,)^a$ is defined

$$f = t_0^b / t_0^a \quad (24)$$

Deformation is imposed on the edges of the sheet, such that

$$D_{22}/D_{11} = \dot{\varepsilon}_{22}/\dot{\varepsilon}_{11} = \rho = const,\ D_{12} = 0,\ W_{12} = 0 \quad (25)$$

where $\dot{\varepsilon}_{22} \equiv D_{22}$ and $\dot{\varepsilon}_{11} \equiv D_{11}$ are the principal logarithmic strain rates, ρ is the strain proportionality constant and W_{ij} are components of the spin tensor. Additionally, $D_{13} = D_{23} = W_{13} = W_{23} = 0$ is assumed, while D_{33} is determined by the plane stress condition ($\dot{\sigma}_{33} = 0$). The evolution of the current groove orientation, Ψ, is given by

$$\tan\Psi = \exp[(1-\rho)\varepsilon_{11}]\tan\Psi_0 \quad (26)$$

Following Hutchinson and Neale [15] [16], the compatibility condition at the band interface is given in terms of the velocity gradient differences inside and outside the band are defined as

$$\boldsymbol{L}_{\alpha\beta}^b = \boldsymbol{L}_{\alpha\beta} + \dot{c}_\alpha n_\beta \quad (27)$$

with the symmetric and skew-symmetric components of the velocity gradient in the band are

$$D_{\alpha\beta}^b = D_{\alpha\beta} + \frac{1}{2}\left(\dot{c}_\alpha n_\beta + n_\alpha \dot{c}_\beta\right), \qquad W_{\alpha\beta}^b = W_{\alpha\beta} + \frac{1}{2}\left(\dot{c}_\alpha n_\beta - n_\alpha \dot{c}_\beta\right) \quad (28)$$

where $\dot{c}_\alpha$ values are the parameters to be determined, and n_α are components of the unit normal vectors to the band orientation given as

$$n_1 = \cos\Psi, \qquad n_2 = \sin\Psi \quad (29)$$

Force equilibrium is established inside and outside of the band by

$$n_\alpha^b \sigma_{\alpha\beta}^b t^b = n_\alpha^a \sigma_{\alpha\beta}^a t^a \quad (30)$$

The sheet thickness inside and outside the band are updated according to

$$\dot{t}^a = D_{33} t^a, \qquad \dot{t}^b = D_{33}^b t^b \quad (31)$$

According to Hutchinson and Neale [15], the onset of localized sheet necking is defined by the ratio of the in-band and out-of-band region exceeding $\dot{\varepsilon}_{33}^b/\dot{\varepsilon}_{33} \geq 10^4$.

4. Results and Discussion

4.1 Material Calibration

The proposed crystallographic transformation model is calibrated to experimental measurements presented in Kim et al. [11] of a TRIP-assisted duplex stainless steel (DSS). The DSS consists of 65% ferrite and 35% retained austenite by volume. Figure 2 presents the initial orientation distribution function (ODF) of the textures for austenite and ferrite.

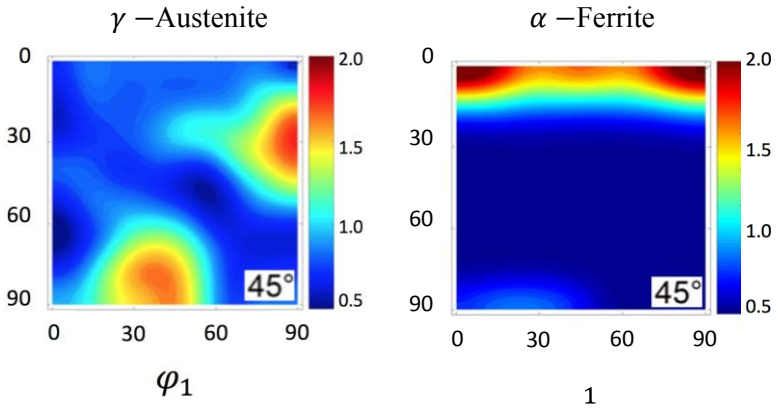


Figure 2. Initial orientation Distribution function of γ −Austenite and α −Ferrite phases of Duplex Stainless Steel obtained from Kim et al. [11]

Table 2 summarizes the calibrated individual phase parameters with the transformation parameters. The elasticity constants of α- ferrite and γ- austenite used in the model were obtained from Fréour et al. [17]. α'- Martensite uses the same elasticity constants as that of α- ferrite, due to crystal similarities. Initially, transformation was turned off and ferrite and austenite response were fit to reduce the number of material parameter. This exclusion of the martensite elastic-plastic behavior focused on the elastic-plastic behavior of ferrite and austenite during the first 10% of deformation. The complete overall response with transformation was calibrated for the martensite elastic-plastic behavior and transformation parameters. The experimental stress strain curve was simultaneously fit with the volume fraction data to obtain martensite parameters and transformation parameters. Figure 3 presents the resulting of the experimental and calibrated stress-strain curves and volume fraction evolution of martensite. Good correlation is achieved between the experimental and calibrated response.

Table 2. Crystal plasticity material parameters for individual phases ($\boldsymbol{C_{t1} = 300, C_{t2} = 24}$)

Phase	$\boldsymbol{C_{11}}$ [GPa]	$\boldsymbol{C_{12}}$ [GPa]	$\boldsymbol{C_{44}}$ [GPa]	$\boldsymbol{h_0}$ [MPa]	$\boldsymbol{m}$	$\boldsymbol{\tau_0}$ [MPa]	$\boldsymbol{q}$	$\boldsymbol{n}$
Ferrite, α	231.4	134.7	116.4	132	0.05	128	1.00	0.15
Martensite, α'	231.4	134.7	116.4	1000	0.05	230	1.00	0.22
Austenite, γ	197.5	124.5	122	95	0.05	95	1.00	0.16

a) Stress-Strain Response b) Volume Fraction Evolution of Martensite

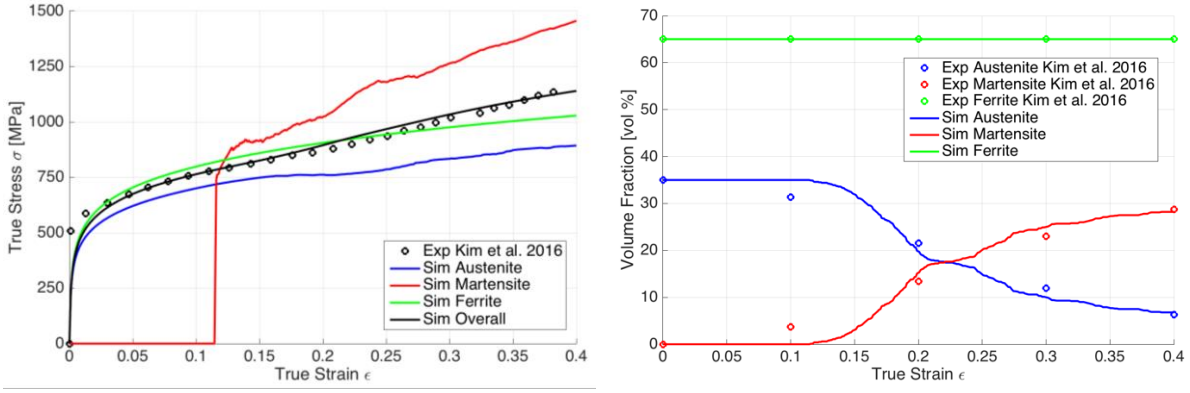


Figure 3. Experimental and calibrated uniaxial a) stress-strain curve and b) phase volume fractions with transformation

4.2 Forming Limit Analysis

The effects of the constitutive and transformation model kinetics on formability are presented and explored for DSS. Each formability study was conducted with a macroscopic strain rate of $D_{11} = 1.0 \times 10^{-3} s^{-1}$, in-plane strain proportionality constant of $-0.5 \leq \rho \leq 1.0$, in $\Delta\rho = 0.1$ increments, initial band angle $0° \leq \Psi_0 \leq 20°$, in $\Delta\Psi_0 = 5°$ increments, and an imperfection parameter of $f = 0.99$. The importance of various transformation kinetics on formability was studied by disabling the constitutive model feature (setting constants to extremely large or small values). Table 3 presents the test matrix that was used to conduct this study. A total of four formability studies were created by simulating the complete TRIP response of DSS, disabling the single variant Bain orientation, disabling transformation kinetics (dual-phase ferrite and austenitic steel), and setting all austenite properties to martensite (dual-phase ferrite and martensite steel).

Table 3. Test Matrix of Transformation Kinetics Study

Sim. #	Simulation Type	Modifications
1	Full Model of DSS	None
2	No Bain Spin	$\varphi_1 = \varphi_1 + 90° \rightarrow \varphi_1 = \varphi_1 + 0°$
3	No Transformation	$C_{t1} = C_{t2} = 10^5$
4	No Austenite Phase	Set all FCC austenite crystal properties to BCC martensite

Figure 4 presents the predicted formability of the DSS without the Bain spin variant, DSS without martensite transformation and austenite material parameters replaced with martensite material parameters. The complete formulation of TRIP for simulating the DSS is also presented for comparison. It should be mentioned that formability predictions with (blue) and without (red) incorporating the Bain variant are coinciding with each other. Figure 5 presents the thinning ratio, stress response, hardening rate and martensite volume fraction evolution inside and outside the band at various load paths for the four simulations studied. The thinning ratio is defined as the ratio between the strain rate outside of the band and inside of the band ($\dot{\varepsilon}_{33}/\dot{\varepsilon}_{33}^{b}$).

Formability of the full TRIP model shows superior formability throughout the entire strain proportionality domain; the full TRIP model shows at least 20% more formability and more than 100% increase in the formability in plane strain tension. This result highlights the significance of TRIP in increasing formability. Until approximately 10% strain, no martensite has formed in the material. Thus, the hardening and necking responses are identical with a steady increase in the thinning ratio. In the full model, martensite begins to evolve that results in an immediate increase in the hardening rate (black arrows in Figure 5). Yet, the hardening rate of the model without transformation continues to decline. This rapid change in the hardening rate stabilizes the localization behavior by a sudden reduction of the thinning ratio which increased the strain to failure (red arrows in Figure 5).

Overall, predictions with (blue) and without (red) incorporating the Bain variant show little to no influence on formability. The complete TRIP formulation shows a slight increase in formability (~0.3% strain) on the drawing side ($\rho < 0$) due to the abrupt rotation that introduces an additional straining mechanism. Cherkaoui et al. [18] has shown that multiple variants of crystallographic orientations for martensite are possible. A further study should be performed that incorporates multiple variant selection schemes of martensite and its impact on formability.

Comparison of the dual phase ferrite-martensite forming limit curve further highlights the advantages of the TRIP mechanism. From uniaxial tension to midway through the stretching regime ($\rho = 0.5$), the full model DSS predicts higher formability. The dual phase ferrite-martensite curve, however, shows superior formability in the biaxial regime. In the TRIP-assisted material, the majority of transformation occurs in the first 20% strain before localization becomes uncontrollable. As such, there was too much martensite generation to suppress necking in an efficient manner. Furthermore, the dual phase ferrite-martensite has 24 slip systems for all crystals compared to the TRIP-enhanced material with 12 slip systems in the FCC phase. The higher number of slip systems leads to a smoother yield locus in the biaxial to plane strain region that produces better formability in the biaxial region [14].

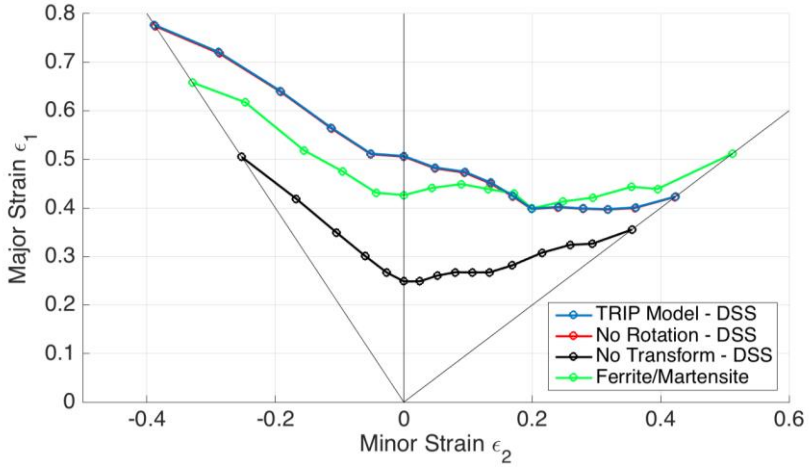


Figure 4. Predicted formability of a) Full Model of DSS, b) No Bain Spin, c) No Martensite Transformation and d) Ferrite and Martensite

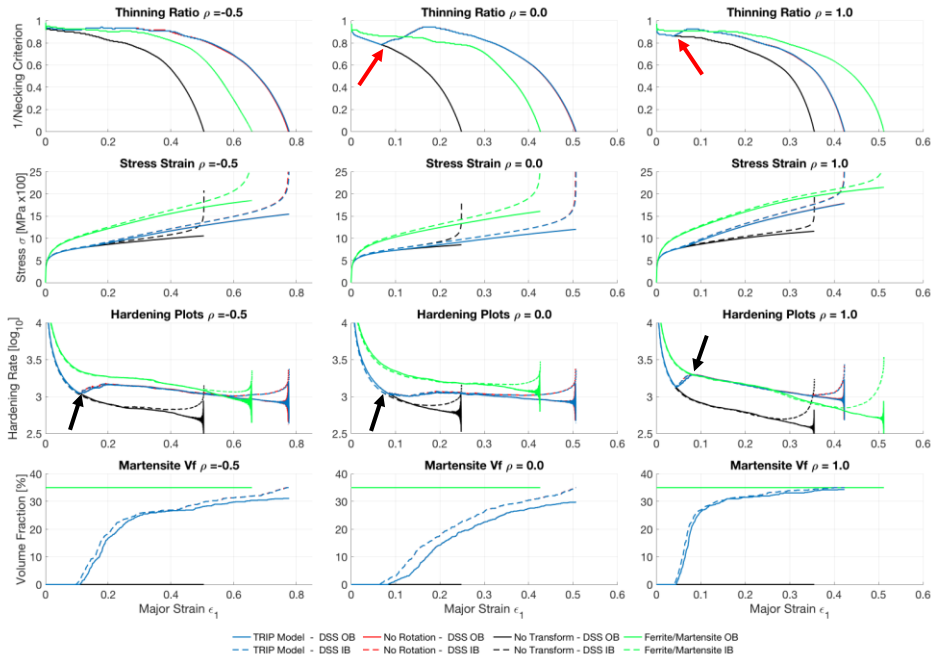


Figure 5. Thinning Ratio, Stress Response, Hardening Rate and Martensite Volume Fraction Evolution vs Out of Band Effective Strain at various load paths for the four simulations studied

5. Conclusions

A Taylor type TRIP crystal plasticity formulation was developed to capture the macro and micro-mechanical response of TRIP assisted multiphase steels for forming. A new stress-based transformation criterion, based on the micromechanics of habit-plane interaction, was developed to initiate transformation. The model was successfully calibrated to the experimental stress-strain and volume fraction evolution presented in Kim et al. [11] for duplex stainless steel. Simulations polycrystalline aggregates were performed to highlight the transformation mechanisms of the TRIP effect for different loading directions. The crystal plasticity framework was implemented into the Marciniak and Kuczynski (MK) [8] framework to simulate the forming limit diagram of the TRIP assisted AHSS. The mechanism of transforming from low strength austenite to high strength martensite showed enhanced formability compared to a material without the mechanism. At least 20% improvement in formability was observed when incorporating the transformation mechanism. This was a result of martensite transformation occurring at a time where it could suppress necking through a sudden increase in hardening rate.

Acknowledgements

Financial support for this work was provided by the Natural Sciences and Engineering Research Council – Industrial Research Chair (NSERC-IRC) under grant no. IRCPJ-503185-2016, and General Motors of Canada.

References

[1] Zackay V, Parker E, Fahr D, and Busch R 1967 *ASM Trans. Quart.* **60**(2) 252-259.
[2] Kohar C, Cherkaoui M, El Kadiri H, and Inal K 2016 *Int. J. Plasticity* **84** 224-254.
[3] Asaro R and Needleman A 1985 *Acta Metall Mater* **33** 923-953.
[4] Inal K, Wu P, and Neale K 2002 *Int J Solids Struct* **39** 3469-3486.
[5] Taylor G 1934 P. R. Soc. Lond. A-Conta. **145**(855) 362-387.
[6] Bain E, and Dunkirk N 1924 *Trans. AIME* **70**(1) 25-47.
[7] Scheil, E 1932 *Zeitschrift für anorganische und allgemeine Chemie,* **207**(1) 21-40.
[8] Marciniak Z, and Kuczynski K 1967 *Int. J. Mech. Sci.* **9**(9) 609-620.
[9] Connolly D, Kohar C, Mishra R, and Inal K 2018 *Int. J. Plasticity*.
[10] Cayron C 2013 *Acta Crystallogr A* **69**(5) 498-509.
[11] Kim E, Woo W, Heo Y, Seong B, Choi J, and Choi S 2016 *Int. J. Plasticity* **79** 48-67.
[12] Peirce D, Shih C, and Needleman A 1984 *Computers and Structures* **18**(5) 875-887.
[13] Wu P, Neale K, and Van der Giessen E 1997 *P. R. Soc. A.* **453** 1813-1848.
[14] Inal K, Neale K, and Aboutajeddine A 2005 *Int J Plasticity* **21** 1255-1266.
[15] Hutchinson J, and Neale K 1978 *Mechanics of Sheet Metal Forming* 127-152.
[16] Hutchinson J, and Neale K 1978 *Mechanics of Sheet Metal Forming* 269-285.
[17] Freour S, Gloaguen D, Francois M, and Guillen R 2003 *Physica Status Solidi (b)* **239**(2) 297-309.
[18] Cherkaoui M, Soluami A, Zeghloul A, and Khaleel M 2008 *Phil Mag* **88**(30-32) 3479-3512.